Supplemental Material

for

Detecting Molecular Rotational Dynamics Complementing the Low-Frequency Terahertz Vibrations in a Zirconium-Based Metal-Organic Framework

Matthew R. Ryder,[1,2,3] Ben Van de Voorde,[4] Bartolomeo Civalleri,[5] Thomas D. Bennett,[6] Sanghamitra Mukhopadhyay,[2] Gianfelice Cinque,[3] Felix Fernandez-Alonso,[2,7] Dirk De Vos,[4] Svemir Rudić,[2] and Jin-Chong Tan[1,*]

[1]*Multifunctional Materials & Composites (MMC) Laboratory, Department of Engineering Science, University of Oxford, Parks Road, Oxford OX1 3PJ, United Kingdom*

[2]*ISIS Facility, Rutherford Appleton Laboratory, Chilton, Didcot OX11 0QX, United Kingdom*

[3]*Diamond Light Source, Harwell Campus, Didcot, Oxford OX11 0DE, United Kingdom*

[4]*Centre for Surface Chemistry and Catalysis, KU Leuven, Arenbergpark 23, Leuven, B-3001, Belgium*

[5]*Department of Chemistry, University of Turin, via Pietro Giuria 7, 10125 Torino, Italy*

[6]*Department of Materials, University of Cambridge, Cambridge CB3 0FS, United Kingdom*

[7]*Department of Physics and Astronomy, University College London, London WC1E 6BT, United Kingdom*

Correspondence to: jin-chong.tan@eng.ox.ac.uk

Table of Contents

1 Materials Synthesis and Characterization

The MIL-140A sample was synthesized according to that reported in Ref. [1], allowing a gram scale synthesis, the material was subsequently post-treated by heating it to reflux with 3 x 600 mL DMF and 3 x 600 mL technical ethanol, followed by calcination at T = 673 K as adopted from Ref. [2].

Before the neutron and synchrotron far-infrared spectroscopy experiments, the purity and crystallinity of the powdered sample were confirmed using powder X-ray diffraction (PXRD).
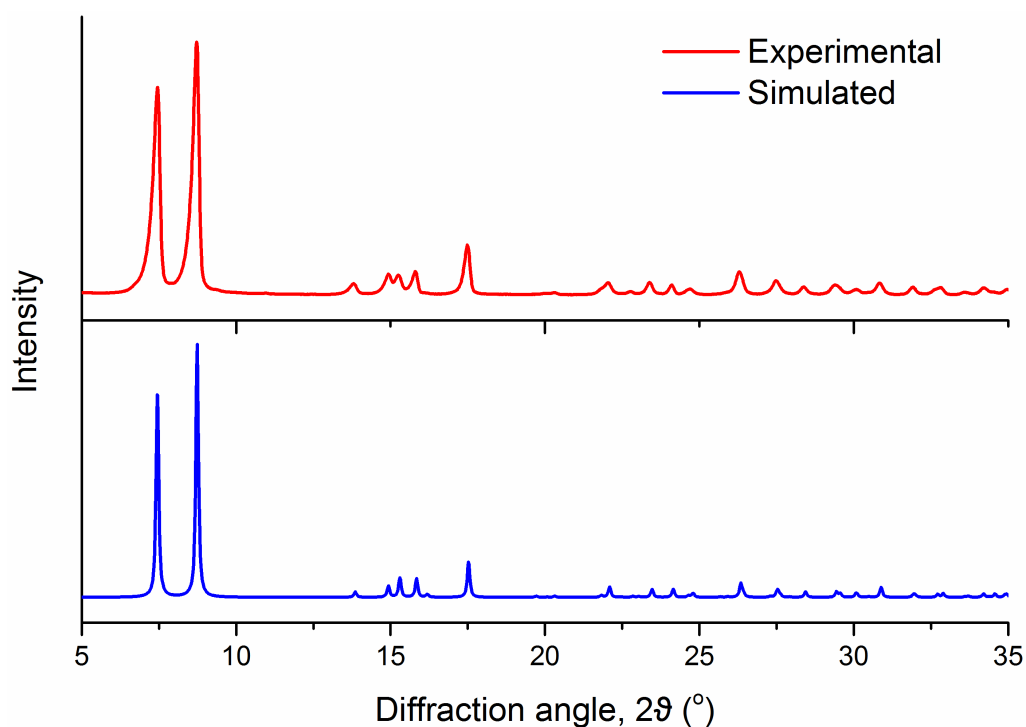
Fig. S1. PXRD of MIL-140A comparing the experimental spectrum for the sample used in the measurements and the simulated spectrum from the CIF file in the literature.

2 Inelastic Neutron Scattering (INS)

The INS spectra were recorded using the TOSCA and OSIRIS spectrometers at the ISIS Pulsed Neutron and Muon Source at the Rutherford Appleton Laboratory (Chilton, UK):

TOSCA is a high resolution (ΔE/E ~1.25%) broadband (0 – 4,000 cm^{-1}) spectrometer [3-7]. It is an indirect geometry time-of-flight spectrometer where a pulsed, polychromatic beam of neutrons collide with the sample at a distance of ~17 m from the source. The scattered neutrons are then Bragg-reflected by a pyrolytic graphite analyser, and higher-order reflections beyond (002) are suppressed by a cooled (T < 50 K) beryllium (Be) filter, to selectively analyse neutrons of a consistent final energy. Therefore, neutrons with a final energy of approximately 32 cm^{-1} (~1 THz) are passed towards the ^{3}He detector bank. The detector array is comprised of a total of ten banks each having thirteen ^{3}He tubes with an effective length 250 mm. Five banks are located in the forward direction (scattering angle ~45º) and five in the backwards direction (~135º). The use of a low (fixed) final energy translates into a direct relationship between energy transfer (E_T, cm^{-1}) and momentum transfer (Q, Å^{-1}) such that $E_T \approx 16Q^2$. Energy transfer and spectral intensity can then be calculated to convert to the conventional $S(Q,\omega)$. A disc chopper is positioned to prevent frame overlap at 8 m from the moderator. It relied on the 40 ms timeframe during the operation of both target stations at ISIS to extend the incident-wavelength bandwidth of the instrument down to -24 cm^{-1} i.e. elastic line region. The sample (~2 g) was wrapped in a 4x4 cm^2 aluminium foil sachet and placed in a thin-walled aluminium can. To reduce the impact of the Debye–Waller factor on the observed spectral intensity and to be comparable with the theoretical spectra, the sample was cooled to approximately 10 K by a closed cycle refrigerator (CCR), and the spectra was recorded for 10 hours.

OSIRIS is a high resolution (25.4 µeV) indirect-geometry neutron spectrometer with long-wavelength diffraction capabilities [8-10]. The secondary spectrometer sits at ~34 m from a 25 K liquid hydrogen cooled moderator. Optimised for low-energy, high-resolution inelastic neutron-scattering studies, OSIRIS uses a broadband of incident wavelengths which are Bragg-scattered from a crystal analyser array following interaction with the sample. Due to utilising a pulsed neutron source, time-of-flight methods are used to determine energies at

each particular scattering angle. When used as a diffractometer in backscattering geometry, its resolution amounts to $\Delta d/d = 2.5 \times 10^{-3}$, where Δd is the resolution in d-spacing.

The Mantid software was used to process and analyse the experimental neutron data [11].

Web links:

http://www.isis.stfc.ac.uk/instruments/tosca

http://www.isis.stfc.ac.uk/instruments/osiris

http://www.mantidproject.org

3 Synchrotron Radiation Far-Infrared (SR-FIR) Absorption and (offline) Raman Spectroscopy

Infrared (IR) absorption spectroscopy experiments were performed at the Multimode InfraRed Imaging and Microspectroscopy (MIRIAM) Beamline (B22) at the Diamond Light Source synchrotron facility [12]. The main advantage of the synchrotron radiation (SR) source was the brightness of the beam (photon flux density several orders of magnitude higher than conventional sources) and broadband spectral range (covering simultaneously from the visible to the sub-THz region). The storage ring was operating in the standard user mode, therefore 900 bunches filling pattern for a total circulating current of 300 mA, topped up every 10 minutes (lifetime circa 18 h and photon flux fluctuation limited to 0.3%). IR spectroscopy was performed in vacuum via a Bruker Vertex 80 V Fourier Transform IR (FTIR) interferometer (Bruker Optics, Ettlingen, Germany) equipped with an RT DLaDTGS detector. The measurements were performed at a resolution of 2 cm^{-1} with a 6 μm thick Mylar broad-band multilayer beamsplitter (allowing for the measurement of the spectral range below 650 cm^{-1}) at a scanner velocity of 10 kHz (with respect to the 15,800 cm^{-1} laser reference). High signal-to-noise SR-FIR spectrum was detected using a liquid helium-cooled bolometer.

The IR experiments were performed at room temperature (RT) using the Attenuated Total Reflection (ATR) method for the advantage of measuring powered samples [13]. Specifically, the sample was placed on top of a diamond ATR crystal and held in position by pressure applied onto a HDPE disk via a clamp mechanism. Schematically, the synchrotron IR beam enters the ATR crystal from the bottom at an angle of approximately 45° and is reflected at the sample, then re-directed via a 45° mirror to the detector pupil. Provided the sample's refractive index be lower than the ATR material (diamond n = 2.4) only a fraction of the radiation reaches into the sample (evanescent wave). At the wavelength where the sample absorbs energy the evanescent wave is attenuated, and consequently, the beam exiting is modulated like in a transmission measurement.

Raman spectroscopy experiments were performed using a Bruker Senterra confocal Raman microscope with a 50× objective and a high numerical aperture of 0.8. The excitation wavelength was 532 nm at 50 mW, with a resolution of 6–9 cm^{-1} controlled by the 1200 lines per mm grating and the spectral range of ~4000 cm^{-1} to 40 cm^{-1} by the edge filter. The spectra were detected by a depleted Si CCD Peltier cooled to −80°C.

4 *Ab Initio* Quantum Mechanical Calculations

Density functional theory (DFT) calculations were performed at the PBE [14] level of theory and corrected with an empirical dispersion term (PBE-D) [15]. All of the calculations were performed with the periodic *ab initio* code CRYSTAL14 [16]. The code considers crystalline orbitals as linear combinations of Bloch functions (BF) and evaluates them using a regular three-dimensional (3D) mesh in the reciprocal space. Each BF was constructed from local atomic orbitals (AOs), which are linear combinations of Gaussian-type functions (GTF) and each GTF is the result of a Gaussian multiplied by a solid spherical harmonic. All electron TZVP basis sets were used for Zr, O, C and H atoms, similar to our previous work on ZIFs [17]. The adopted basis sets contain 1,264 basis functions, corresponding to 528 electrons spread over 616 shells per unit cell.

The lattice parameters and atomic coordinates were both optimised (maintaining the symmetry space group) via a quasi-Newtonian algorithm in which the quadratic step (BFGS Hessian updating scheme) is combined with a linear one [18-22]. Convergence was tested on the root mean square (RMS) and the absolute value of the largest component of the gradients and the estimated displacements. The threshold for the maximum and RMS gradient, and the maximum and RMS atomic displacement of all atoms was set to 1.5×10^{-4}, 1.0×10^{-4}, 3.0×10^{-4} and 2.0×10^{-4} a.u., respectively. The optimisation was considered to have completed when all four conditions were simultaneously satisfied.

The mass-weighted Hessian matrix for the calculation of the vibrational frequencies was obtained by numerical differentiation of the analytical first derivatives, calculated at geometries obtained by slightly displacing, in turn, each of the 3N nuclear coordinates with respect to the equilibrium geometry. Eckart conditions were imposed to the Hessian to reduce numerical noise. Vibrational frequencies were calculated at the Γ point, as the volume of each system is sufficient to expect negligible phonon dispersion.

The IR intensities have been computed through the Berry Phase approach [23], by evaluating the Born atomic tensors as polarization differences between the original and the distorted geometries. This method assumes the polarization difference is equal to the time-

integrated transient macroscopic current that flows through the sample during the vibrations [16, 24].

The Raman intensities were calculated analytically via a Coupled-Perturbed Hartree-Fock / Kohn-Sham (CPHF) approach [25, 26]. The theoretical spectra was then corrected for the experimental conditions (293 K and 532 nm) by multiplying with the prefactor *C*:

$$C \sim (\omega_L - \omega_i)^4 \frac{1 + n(\omega_i)}{30\omega_i}$$

where $n(\omega_i)$ is the Bose occupancy factor.

Summarized below are the comparisons of lattice parameters calculated from DFT (for ideal crystalline structures) versus experimental values reported in the literature [27]. We show that the PBE-D structure is in better agreement with the OSIRIS experimental diffraction data (see Fig. S3).

MIL-140A (*C 2/C*)					
Method	*Lattice parameters* (Å)				*Volume* (Å^3)
	a	*b*	*c*	*β*	
Experimental CIF	24.424	11.180	7.802	103.86	2130.41
PBE	24.890	11.276	7.980	102.66	2239.66
PBE-D	24.907	11.258	7.828	104.45	2194.99
• Average difference in experimental and theoretical lattice parameters for PBE: 1.55% • Average difference in experimental and theoretical lattice parameters for PBE-D: 0.89%					

5 OSIRIS low-energy high-resolution inelastic neutron-scattering & diffraction data
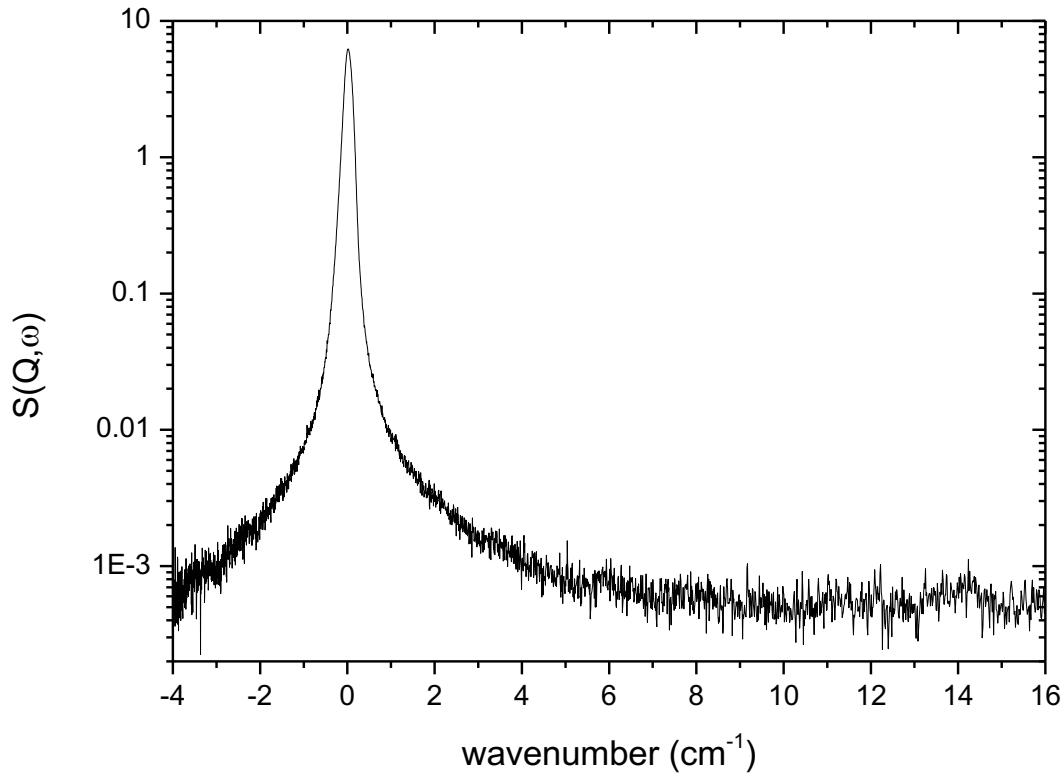
Fig. S2. The low energy INS spectrum of the MIL-140A near the elastic line recorded with the help of OSIRIS neutron spectrometer at the temperature of 5K. The spectrum intensity has been calibrated with the help of the vanadium sample and highlights the absence of the vibrational modes in the corresponding low wavenumber region.
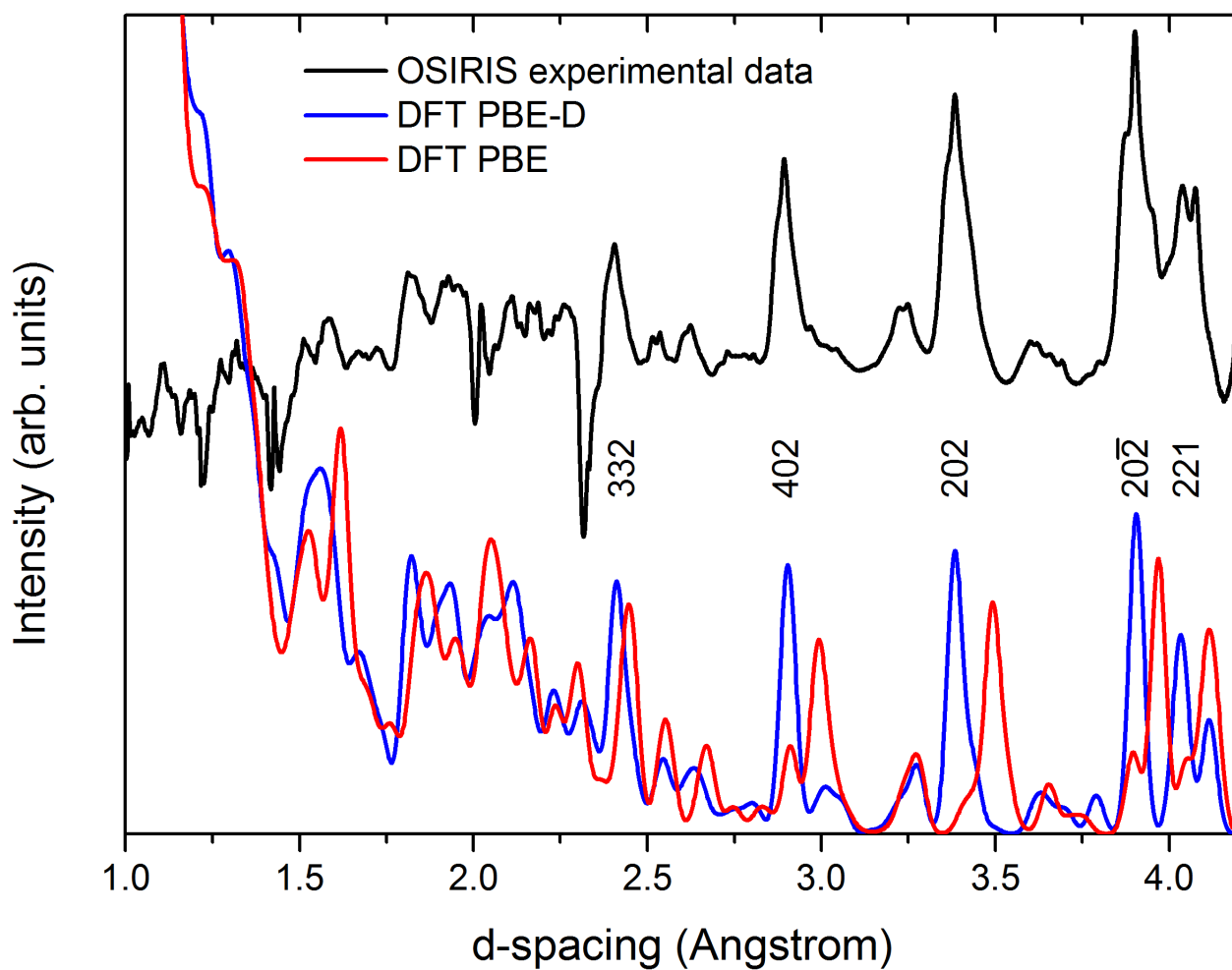
Fig. S3. Neutron diffraction data measured using the OSIRIS instrument, compared to the predicted pattern from the MIL-140A structure obtained by DFT PBE and PBE-D level of theory (§4). It can be seen that the peaks derived from DFT PBE-D is in better agreement with the experimental OSIRIS data.

6   INS data in the range of 200 - 4,000 cm^{-1}
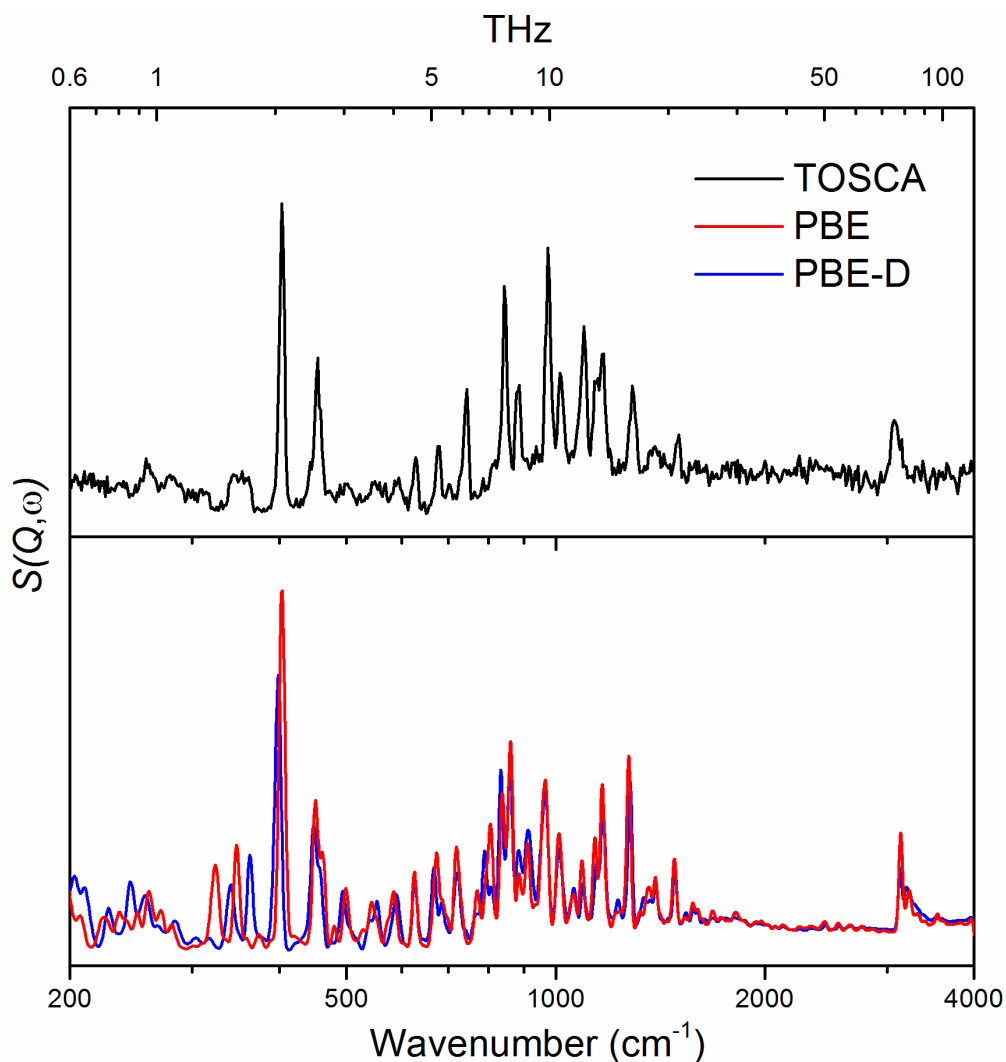
Fig. S4. Comparison of experimental and theoretical INS spectra in the 200-4,000 cm^{-1} range (log scale). The theoretical spectrum includes overtones to the 10th order, calculated using the aClimax software [28].

We have identified new characteristic frequencies for semi-local motions such as organic linker and metal polyhedra deformations, as follows: 625-854 cm^{-1} for phenyl ring deformation; 486-595 cm^{-1} for Zr-O stretching of polyhedra. Furthermore we compared the experimental mid-IR with theory, allowing us to explain every region of the INS spectra, corresponding to 'local' motions, as follows: 3123-3138 cm^{-1}, aromatic C-H stretching; 1281-1604 cm^{-1}, C-H bending; 1481-1543 cm^{-1}, C-O stretching; 1347-1429 cm^{-1}, C-C stretching; 859-1281 cm^{-1}, C-C stretching and C-O bending modes.

7 Comparison of PBE and B3LYP with experimental INS data
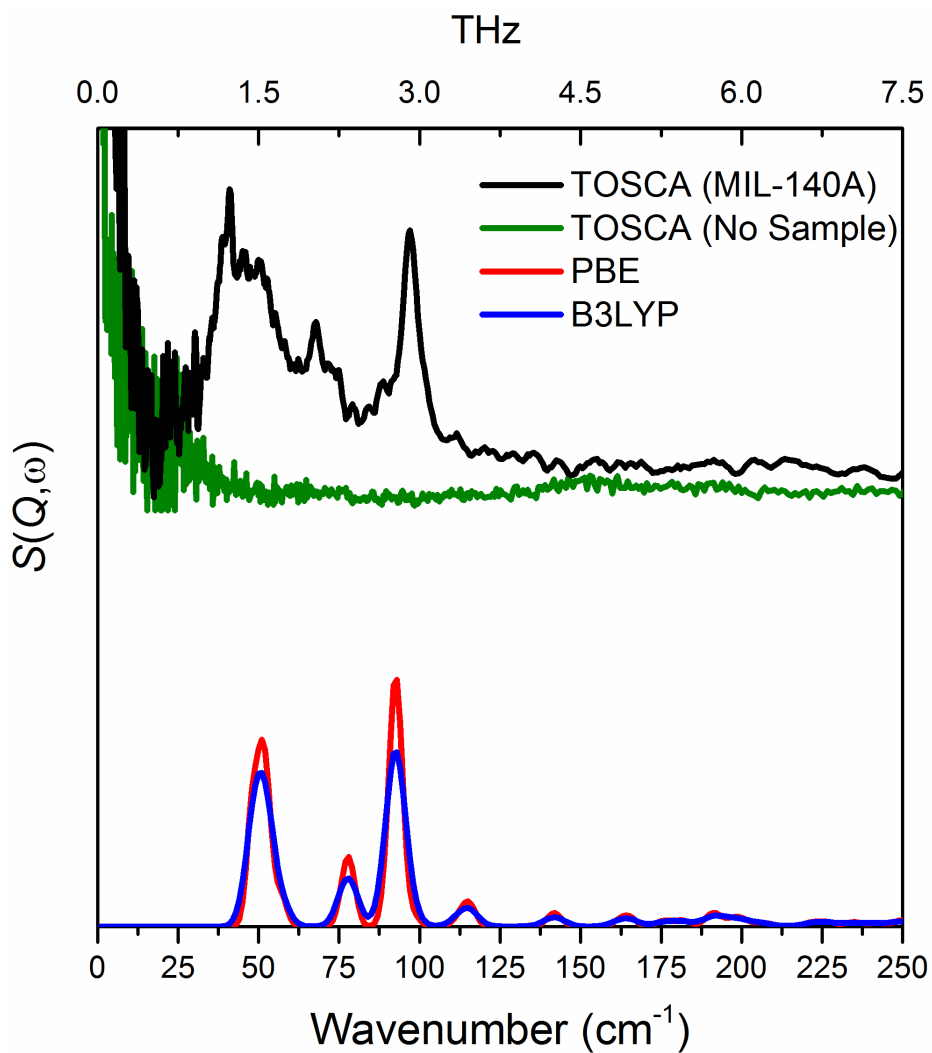
Fig. S5. Comparison of the theoretical spectra obtained at the PBE and B3LYP levels of theory with experimental INS spectra in the 0-250 cm^{-1} region. The spectra show that there is a negligible difference observed between the two levels of density functional theory.
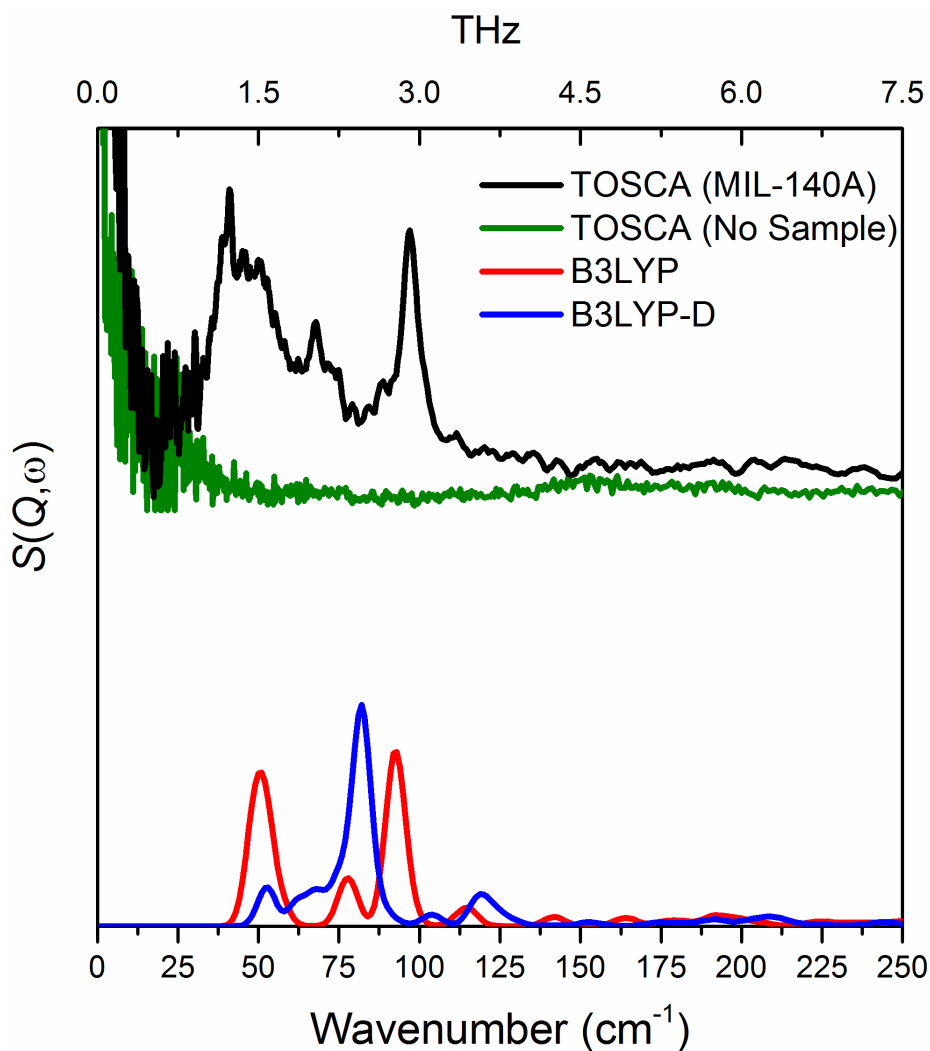
Fig. S6. Comparison of the theoretical spectra obtained at the B3LYP and B3LYP-D levels of theory with experimental INS spectra in the 0-250 cm^{-1} region. The spectra show that the Grimme-D2 dispersion correction does not produce an accurate theoretical INS spectra at the B3LYP level, likely due to over-binding.
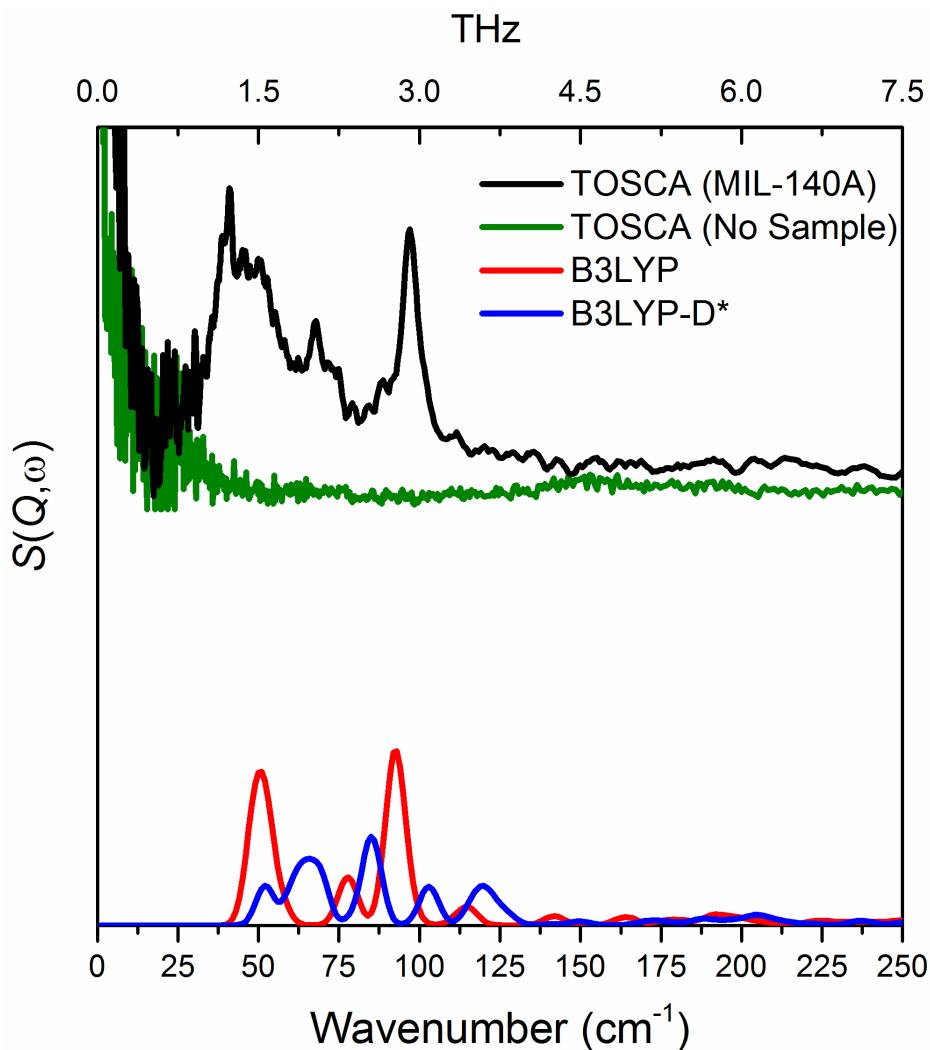
Fig. S7. Comparison of the theoretical spectra obtained at the B3LYP and B3LYP-D* [29] levels of theory with experimental INS spectra in the 0-250 cm^{-1} region. The spectra show that even using the dampened dispersion correction, designed to improve the agreement in crystal structures, still does not produce as accurate a theoretical INS spectra as we report in the manuscript at the PBE-D level of theory.

8 Nature of THz Vibrational Modes < 650 cm^{-1} (~19.5 THz)

IRREP = Irreducible representation; IP = in-plane; OP = out-of-plane

Table S1: Assignment of IR-active vibrational modes up to 650 cm^{-1}.

Mode (cm^{-1})	IRREP	Description
48.1583	**Bu**	**All Linker Trampoline Motion**
48.1589	**Au**	**Type A Linker Trampoline Motion**
53.62	**Bu**	**All Linker Trampoline Motion**
58.05	**Au**	**Type B Linker Rotor**
90.25 95.69	Bu Bu	Polyhedra Deformation and Rigid Linker Rocking
97.66	Au	Polyhedra Deformation and Type A linker Translational Motion
119.16	Bu	Rigid Linker Rocking and Polyhedra Deformation
130.06	Au	Polyhedra Deformation
146.93	Bu	Rigid Linker IP Rocking and Polyhedra Deformation
162.23	Au	Type A Linker Translational Motion and Polyhedra Deformation
178.70	Bu	Rigid Linker Rocking and Polyhedra Deformation
183.95	Au	Type A Linker Translational motion and Polyhedra Deformation
192.56 195.62	Bu Au	Polyhedra Deformation
203.63	Bu	Type B IP Rocking and Polyhedra Deformation
209.84	Au	Type A Linker Translational motion and Polyhedra Deformation
214.10 226.90	Bu Au	Polyhedra Deformation
244.50 256.90	Bu Bu	Strong OP Aromatic Ring Rocking of the Type B linkers and weaker OP rocking of the Type A linkers
260.75	Bu	Zr-O stretching and C-C stretching of the Type A linkers (Linker Translational motion and Polyhedra Deformation) along with OP Aromatic Ring Rocking of the Type B linkers

272.36	Au	Zr-O-C Bending not including the Type B linkers (Polyhedra Deformation)
281.20	Au	Symmetric Zr-O stretching and C-C stretching (Linker Translational motion and Polyhedra Deformation)
287.36	Bu	Zr-O-C Bending (Polyhedra Deformation)
340.29	Au	Zr-O-Zr Buckling (Polyhedra Deformation)
363.67	Bu	IP Aromatic Ring Rocking of just the Type B linkers
379.81 381.05 392.04	Bu Au Au	Zr-O-Zr Buckling (Polyhedra Deformation)
394.31	Au	Strong OP Aromatic Ring Deformation of just the Type B linkers
399.91 400.41	Bu Au	Strong OP Aromatic Ring Deformation not including Type B linkers
426.67	Au	Asymmetric Zr-O stretching and C-C stretching of just the Type B linker (IP Aromatic Ring Deformation)
446.75	Bu	OP Aromatic Ring Deformation of all rings
448.48	Au	OP Aromatic Ring Deformation not including Type B linkers
450.39 475.70	Bu Bu	OP Aromatic Ring Deformation of all rings
493.51	Bu	Zr-O-Zr Stretching (Polyhedra Deformation)
536.33	Au	Zr-O stretching and C-C stretching of just the Type A linker (Linker Translational motion)
539.49 548.20	Bu Bu	Zr-O stretching of just the Type A Linkers
555.65	Au	Symmetric Zr-O stretching and C-C stretching of just the Type B linker (Linker Translational motion)
563.01	Au	Zr-O stretching of just the Type A Linkers
587.46 595.04	Bu Bu	Zr-O stretching of just the Type B Linkers
625.25	Bu	IP Aromatic Ring Deformation of just the Type B linkers

Table S2: Assignment of Raman-active vibrational modes up to 650 cm^{-1}.

Mode (cm-1)	IRREP	Description
44.69 **49.22**	**Bg** **Ag**	**Type A Linker Rotor**
77.19 81.05	Bg Bg	Polyhedra Deformation and Linker Rocking
82.47	**Ag**	**Shear Deformation**
91.76	**Bg**	**Type B Linker Trampoline Motion**
94.19	**Ag**	**Type B Linker Rotor**
114.30 118.43	Ag Bg	OP Linker Rocking and Polyhedra Deformation
144.50	Ag	Type A Linker Rocking and Polyhedra Deformation with Type B Linker Translational Motion
145.14	Bg	OP Linker Rocking and Polyhedra Deformation
168.92	Ag	Type A Linker Rocking and Polyhedra Deformation
169.65	Bg	Type A Linker Rocking and Polyhedra Deformation with Type B Linker Rotating
177.61	Ag	Non-rigid Linker Rocking and Polyhedra Deformation
186.29	Bg	Rigid Linker IP rocking and Polyhedra Deformation
196.86	Bg	Polyhedra Deformation with Rigid Linker Trampoline Motion
202.98	Bg	Polyhedra Deformation
204.96	Ag	Non-rigid Linker OP rocking and Polyhedra Deformation
227.65 228.00	Bg Ag	Polyhedra Deformation and OP rocking of the Aromatic linkers
244.93	Bg	Zr-O-Zr Buckling (Polyhedra Deformation) and OP rocking of the Aromatic linkers
252.48	Ag	Rigid Linker Translational motion and Polyhedra Deformation along with OP Aromatic Ring Rocking of the non-rigid linkers
257.16	Bg	Strong OP Aromatic Ring Rocking of the non-rigid linkers and weaker OP rocking of the Rigid linkers
267.43	Ag	Zr-O stretching and C-C stretching of the rigid linkers (Linker Translational motion and Polyhedra Deformation) along with OP Aromatic Ring Rocking of the non-rigid linkers
275.98	Bg	Zr-O-C Bending of just the rigid linkers (Polyhedra Deformation)
285.05	Ag	OP Aromatic Ring Rocking not including rigid linkers and Polyhedra Deformation
318.48 337.23 342.51	Bg Ag Bg	IP Aromatic Ring Rocking not including rigid linkers

S17

350.41	Ag	Zr-O-Zr Buckling (Polyhedra Deformation)
363.19	Bg	IP Aromatic Ring Rocking of just the rigid linkers
372.75	Bg	Zr-O-Zr Buckling (Polyhedra Deformation)
396.00	Bg	Symmetric Zr-O stretching and C-C stretching of just the rigid linker (IP Aromatic Ring Deformation)
399.41	Ag	Strong OP Aromatic Ring Deformation of just the rigid linkers
430.38	Ag	Symmetric Zr-O stretching and C-C stretching of just the rigid linker (IP Aromatic Ring Deformation)
437.20	Bg	OP Aromatic Ring Deformation of just the rigid linkers
454.31	Ag	Symmetric Zr-O stretching and C-C stretching of just the non-rigid linker (IP Aromatic Ring Deformation)
460.02	Bg	OP Aromatic Ring Deformation of just the rigid linkers
486.01	Ag	Zr-O-Zr Stretching (Polyhedra Deformation)
553.31	Ag	Asymmetric Zr-O stretching and C-C stretching of just the rigid linker (Linker Translational motion)
556.28	Bg	Zr-O stretching of just the Rigid Linkers
578.27	Ag	Zr-O stretching of just the non-Rigid Linkers
588.04 594.74	Bg Bg	Zr-O stretching of all the linkers
626.34	Bg	IP Aromatic Ring Deformation of all rings
626.45	Ag	IP Aromatic Ring Deformation not including rigid linkers
627.04	Bg	IP Aromatic Ring Deformation of all rings
632.22	Ag	Zr-O-Zr Stretching (Polyhedra Deformation)

9 Video Clips of Specific Important THz Modes
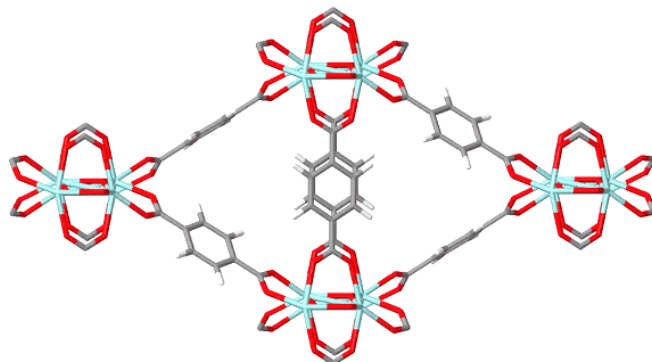
1.34 THz (44.69 cm^{-1}) – Asymmetric Type-A Linker Rotor

http://www.eng.ox.ac.uk/tan/thz_mil140a/type_a_rotor
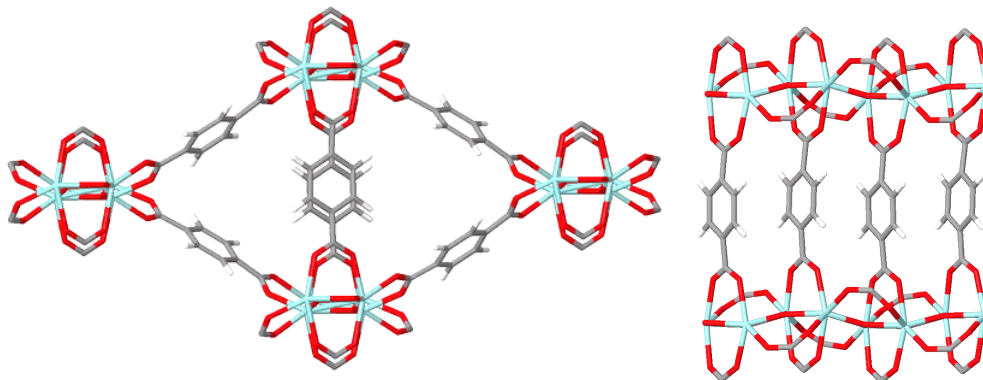
1.44 THz (48.1583 cm^{-1}) – All Linker Trampoline Motion

http://www.eng.ox.ac.uk/tan/thz_mil140a/all_trampoline
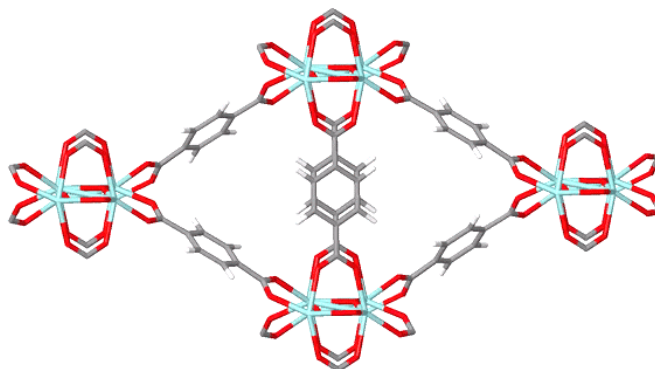
1.44 THz (48.1589 cm^{-1}) – Type-A Linker Trampoline Motion

http://www.eng.ox.ac.uk/tan/thz_mil140a/type_a_trampoline
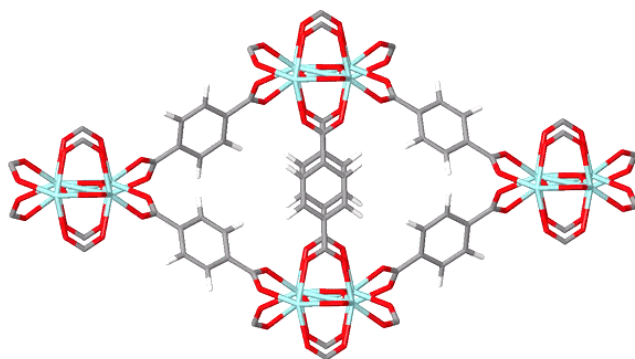
1.48 THz (49.22 cm^{-1}) – Symmetric Type-A Linker Rotor

http://www.eng.ox.ac.uk/tan/thz_mil140a/1-48thz_type_a_rotor
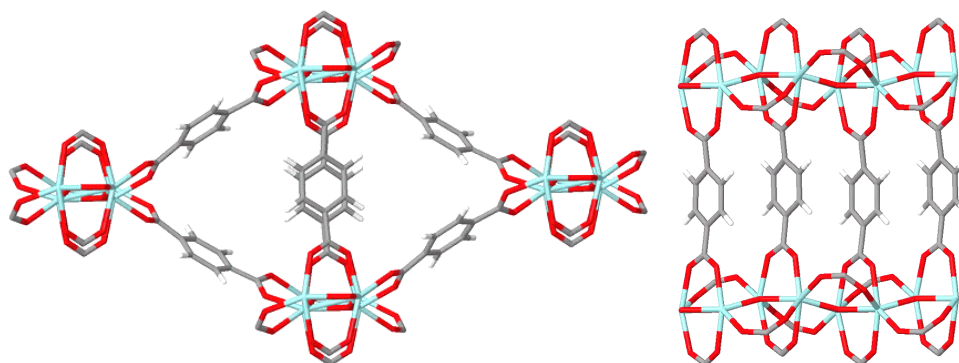
1.61 THz (53.62 cm^{-1}) – All Linker Trampoline Motion

http://www.eng.ox.ac.uk/tan/thz_mil140a/1-61thz_all_trampoline
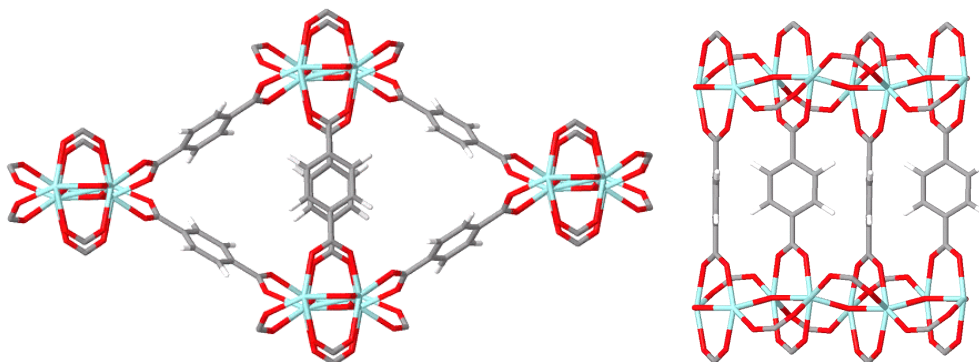
1.74 THz (58.05 cm^{-1}) – Asymmetric Type-B Linker Rotor

http://www.eng.ox.ac.uk/tan/thz_mil140a/1-74thz_type_b_rotor
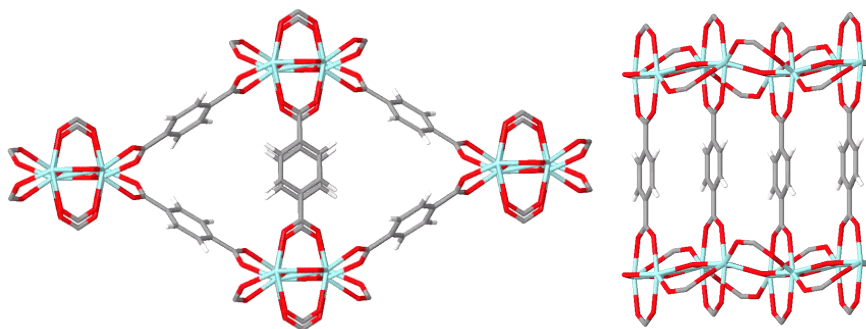
2.47 THz (82.47 cm^{-1}) – Shear Deformation

http://www.eng.ox.ac.uk/tan/thz_mil140a/2-47thz_shear
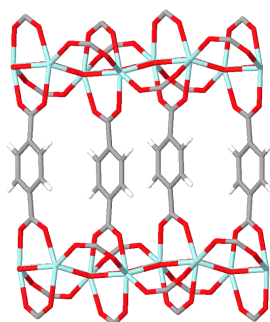
2.75 THz (91.76 cm^{-1}) – Type-B Linker Trampoline Motion

http://www.eng.ox.ac.uk/tan/thz_mil140a/2-75thz_type_b_trampoline
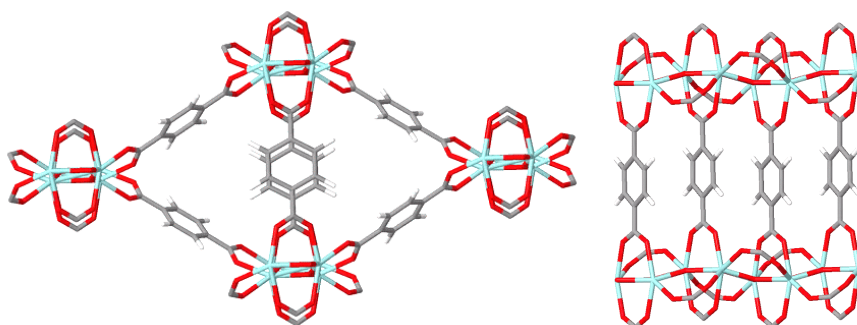
2.82 THz (94.19 cm^{-1}) – Symmetric Type-B Linker Rotor

http://www.eng.ox.ac.uk/tan/thz_mil140a/2-82thz_type_b_rotor

In addition, all DFT calculated modes can be seen at the following link, hosted at the University of Turin. (NB. This requires web browser with Javascript enabled capability):

http://www.crystal.unito.it/vibs/mil-140a

10 Energetics and Solvent Accessible Volume Changes of Type-A and -B Rotors
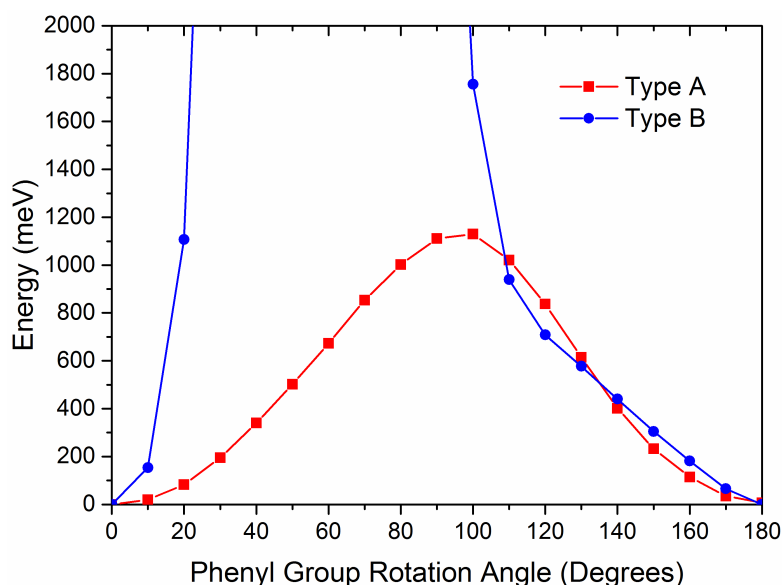
Fig. S5. Comparison of the energy barriers of full Type-A and Type-B linker rotation. Highlighting a similar energy change between 110°-180°, hence a similar response until the Type-B linkers overlapped.
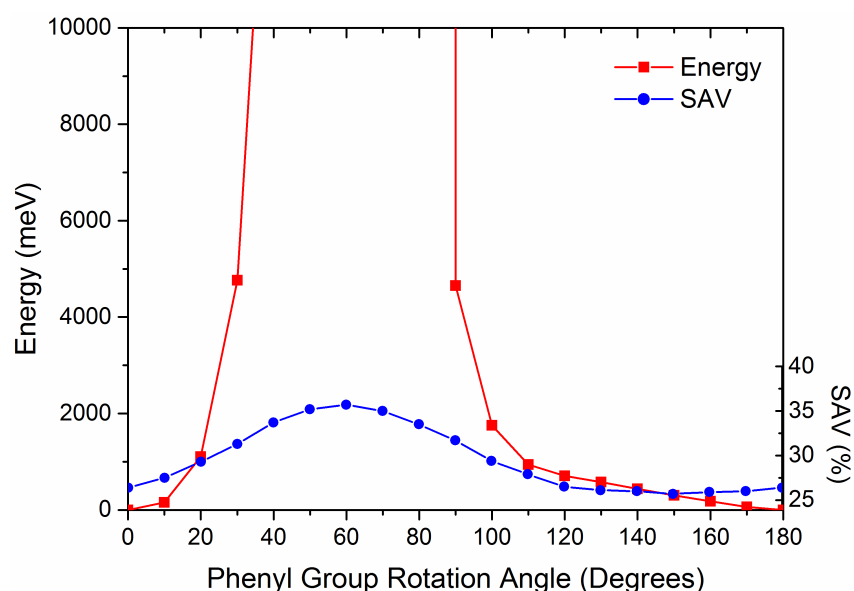
Fig. S6. Comparison of the energy barrier and solvent assessable volume (SAV) changes for a full Type-B linker rotation. Highlighting that the significant increase in SAV is a direct result of the overlapping Type-B linkers.

11 Additional Trampoline Modes Involving All Linkers
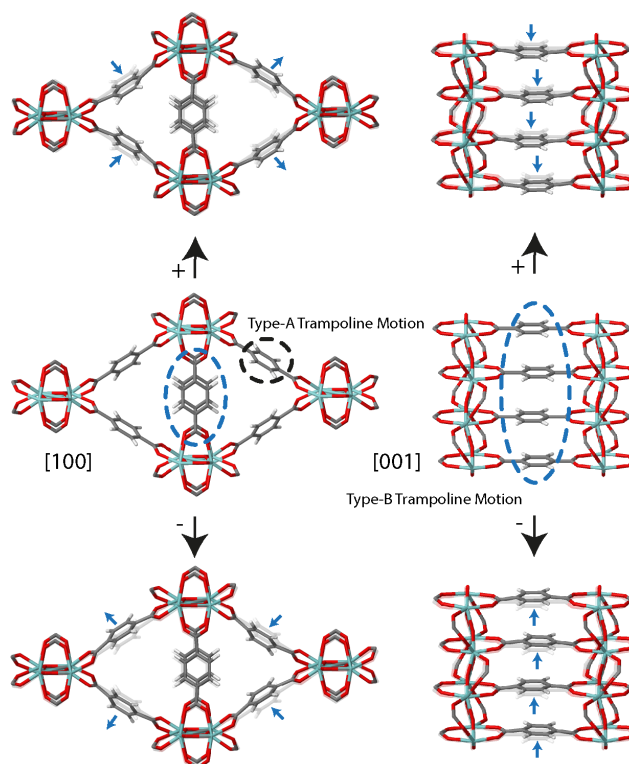
Fig. S7. Simultaneous Type-A and Type-B Trampoline motions of MIL-140A at 48.16 cm^{-1} (1.44 THz).
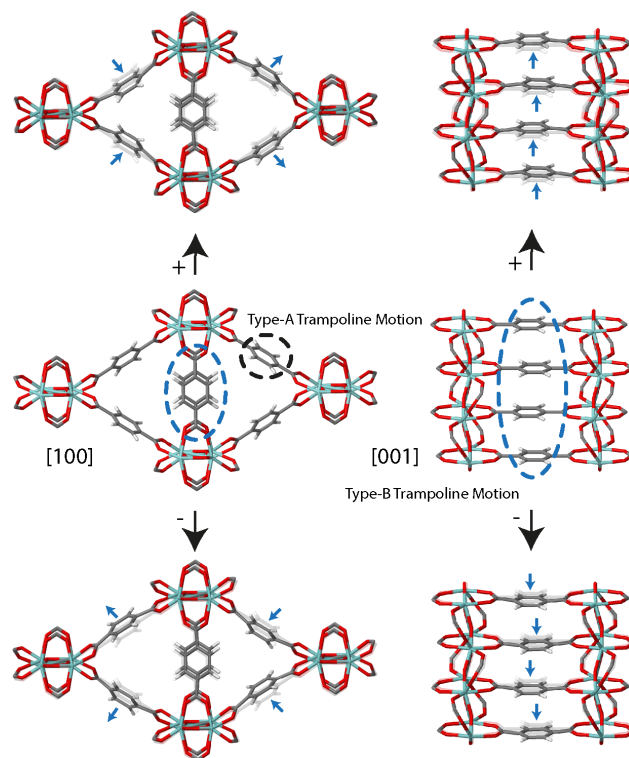
Fig. S8. Simultaneous Type-A and Type-B Trampoline motions of MIL-140A at 53.62 cm^{-1} (1.61 THz).

12 References

1. Liang, W.B., R. Babarao, and D.M. D'Alessandro, *Microwave-assisted solvothermal synthesis and optical properties of tagged MIL-140a metal-organic frameworks.* Inorg. Chem., 2013. **52**(22): 12878.

2. Van de Voorde, B., et al., *Isolation of renewable phenolics by adsorption on ultrastable hydrophobic MIL-140 metal-organic frameworks.* ChemSusChem, 2015. **8**(18): 3159.

3. Colognesi, D., et al., *TOSCA neutron spectrometer: The final configuration.* Appl. Phys. A-Mater., 2002. **74**: S64.

4. Bowden, Z.A., et al., *The TOSCA incoherent inelastic neutron spectrometer: Progress and results.* Physica B, 2000. **276**: 98.

5. Parker, S.F., et al., *TOSCA: A world class inelastic neutron spectrometer.* Physica B, 1997. **241**: 154.

6. Parker, S.F., et al., *Recent and future developments on TOSCA at ISIS.* J. Phys. Conf. Ser., 2014. **554**.

7. Pinna, R.S., et al., *Monte carlo simulations of the TOSCA spectrometer: Assessment of current performance and future upgrades.* EPJ Web. Conf., 2015. **83**: 03013.

8. Telling, M.T.F., et al., *Correction: Spectroscopic characteristics of the OSIRIS near-backscattering crystal analyser spectrometer on the ISIS pulsed neutron source.* Phys. Chem. Chem. Phys., 2016. **18**(11): 8243.

9. Demmel, F., et al., *Opening the terahertz window on the OSIRIS spectrometer.* EPJ Web of Conferences, 2015. **83**: 03003.

10. Andersen, K.H., D.M.Y. Marero, and M.J. Barlow, *The OSIRIS diffractometer and polarisation-analysis backscattering spectrometer.* Appl. Phys. A-Mater., 2002. **74**(0): S237.

11. Arnold, O., et al., *Mantid—data analysis and visualization package for neutron scattering and sr experiments.* Nuclear Instruments and Methods in Physics Research Section A: Accelerators, Spectrometers, Detectors and Associated Equipment, 2014. **764**: 156.

12. Cinque, G., et al., *Multimode infrared imaging and microspectroscopy (miriam) beamline at diamond.* Synchrotron Radiation News, 2011. **24**(5): 24.

13. Haussuhl, E., et al., *Structure-property relations and thermodynamic properties of monoclinic petalite, lialsi4o10.* J Phys Condens Matter, 2012. **24**(34): 345402.

14. Perdew, J.P., K. Burke, and M. Ernzerhof, *Generalized gradient approximation made simple.* Physical Review Letters, 1996. **77**(18): 3865.

15. Grimme, S., *Semiempirical gga-type density functional constructed with a long-range dispersion correction.* J. Comput. Chem., 2006. **27**(15): 1787.

16. Dovesi, R., et al., *CRYSTAL14: A program for the ab initio investigation of crystalline solids.* Int. J. Quantum Chem., 2014. **114**(19): 1287.

17. Ryder, M.R., et al., *Identifying the role of terahertz vibrations in metal-organic frameworks: From gate-opening phenomenon to shear-driven structural destabilization.* Phys Rev Lett, 2014. **113**(21): 215502.

18. Broyden, C.G., *The convergence of a class of double-rank minimization algorithms 1. General considerations.* IMA Journal of Applied Mathematics, 1970. **6**(1): 76.

19. Broyden, C.G., *The convergence of a class of double-rank minimization algorithms: 2. The new algorithm.* IMA Journal of Applied Mathematics, 1970. **6**(3): 222.

20. Fletcher, R., *A new approach to variable metric algorithms.* Computer Journal, 1970. **13**(3): 317.

21. Goldfarb, D., *A family of variable-metric methods derived by variational means.* Mathematics of Computation, 1970. **24**(109): 23.

22. Shanno, D.F., *Conditioning of quasi-newton methods for function minimization.* Mathematics of Computation, 1970. **24**(111): 647.

23. Noel, Y., et al., *Polarization properties of zno and beo: An ab initio study through the berry phase and wannier functions approaches.* Phys. Rev. B, 2001. **65**(1).

24. Dovesi, R., et al., *CRYSTAL14 user's manual, university of torino, torino*, 2014.

25. Maschio, L., et al., *Ab initio analytical raman intensities for periodic systems through a coupled perturbed hartree-fock/kohn-sham method in an atomic orbital basis. I. Theory.* J. Chem. Phys., 2013. **139**(16): 164101.

26. Maschio, L., et al., *Ab initio analytical raman intensities for periodic systems through a coupled perturbed hartree-fock/kohn-sham method in an atomic orbital basis. II. Validation and comparison with experiments.* J. Chem. Phys., 2013. **139**(16): 164102.

27. Guillerm, V., et al., *A series of isoreticular, highly stable, porous zirconium oxide based metal-organic frameworks.* Angew Chem Int Ed Engl, 2012. **51**(37): 9267.

28. Ramirez-Cuesta, A.J., *Aclimax 4.0.1, the new version of the software for analyzing and interpreting ins spectra.* Comput. Phys. Commun., 2004. **157**(3): 226.

29. Civalleri, B., et al., *B3LYP augmented with an empirical dispersion term (B3LYP-D*) as applied to molecular crystals.* CrystEngComm, 2008. **10**(4): 405.